



This is the **submitted version** of the journal article:

Zhang, Chaoqi; Du, Ruifeng; Jacas Biendicho, Jordi; [et al.]. «Tubular CoFeP@CN as a Mott-Schottky catalyst with multiple adsorption sites for robust lithium—sulfur batteries». Advanced Energy Materials, Vol. 11, issue 24 (June 2021), art. 2100432. DOI 10.1002/aenm.202100432

This version is available at https://ddd.uab.cat/record/271937 under the terms of the $\bigcirc^{\mbox{\footnotesize{IN}}}$ license

Tubular CoFeP@CN as a Mott-Schottky Catalyst with Multiple Adsorption

Sites for Robust Lithium-Sulfur Batteries

Chaoqi Zhang⁺, Ruifeng Du⁺, Jordi Jacas Biendicho, Mingjie Yi, Ke Xiao, Dawei Yang, Ting Zhang, Xiang Wang, Jordi Arbiol, Jordi Llorca, Yingtang Zhou*, Joan Ramon Morante, Andreu Cabot*

C. Q. Zhang, R. F. Du, Dr. J. J. Biendicho, X. Ke, D. W. Yang, X. Wang, Prof. J. R. Morante, Prof. A. Cabot

Catalonia Institute for Energy Research - IREC, Sant Adrià de Besòs, Barcelona, 08930, Spain

Email: acabot@irec.cat

C. Q. Zhang, R. F. Du, X. Ke, D. W. Yang, X. Wang, Prof. J. R. Morante Department of Electronic and Biomedical Engineering Universitat de Barcelona, 08028 Barcelona, Spain

M. J. Yi

State Key Laboratory of Advanced Welding and Joining, Harbin Institute of Technology, Shenzhen 518055, China.

T. Zhang, Prof. J. Arbiol
Catalan Institute of Nanoscience and Nanotechnology (ICN2)
CSIC and BIST, Campus UAB, Bellaterra, 08193 Barcelona, Spain

Prof. J. Llorca

Institute of Energy Technologies, Department of Chemical Engineering and Barcelona Research Center in Multiscale Science and Engineering Universitat Politècnica de Catalunya, EEBE, 08019 Barcelona, Spain

Prof. Y. T. Zhou

Key Laboratory of Health Risk Factors for Seafood and Environment of Zhejiang Province, Institute of Innovation & Application

Zhejiang Ocean University, Zhoushan, Zhejiang Province, 316022, China

Email: zhouyingtang@zjou.edu.cn

Prof. J. Arbiol, Prof. A. Cabot ICREA

Pg. Lluís Companys 23, 08010 Barcelona, Spain

⁺ These authors contribute equally to this work

^{*} Corresponding authors

Abstract

The shuttle effect and the sluggish reaction kinetics of lithium polysulfide (LiPS) seriously compromise the performance of lithium-sulfur batteries (LSBs). To overcome these limitations and enable the fabrication of robust LSBs, here we propose the use of bimetallic phosphide CoFeP nanocrystals supported on carbon nitride tubular (t-CN) nanostructures as sulfur hosts. Density functional theory calculations and experimental data confirm that CoFeP@CN composites are characterized by a suitable electronic structure and charge rearrangement that allows them to act as a Mott-Schottky catalyst to accelerate LiPS conversion. Besides, the tubular geometry of CoFeP@CN composites facilitates the diffusion of Li ions, accommodates volume change during the reaction, and offers a huge surface area with abundant lithiophilic/sulfiphilic sites to effectively trap soluble LiPS. As a result, S@CoFeP@CN electrodes deliver high initial capacities of 1607 mAh g⁻¹ at 0.1 C, superior rate performance of 630 mAh g⁻¹ at 5 C, and remarkable cycling stability with 90.44% capacity retention over 700 cycles at 3 C. We further produce coin cells with high sulfur loading, 4.1 mg cm⁻², and pouch cells with 0.1 Ah capacity to validate their superior cycling stability. In addition, we demonstrate here that CoFeP@CN hosts greatly alleviate the often overlooked issues of low energy efficiency and serious self-discharging in LSBs.

Introduction

Lithium-sulfur batteries (LSBs) are regarded as the most promising candidate to replace lithium-ion batteries (LIBs) in next-generation energy storage systems. Compared with LIBs, LSBs are characterized by a sixfold higher theoretical energy density, 2600 W h kg⁻¹, and a potentially lower cost and environmental impact if properly selecting the cathode materials.^[1,2,X] Despite these attractive advantages, the electrically insulating character of sulfur and the shuttle effect of intermediate lithium polysulfides (LiPS) greatly limit the practical application of LSBs.^[3] Additionally, the serious volume changes and slow redox kinetics during the charging/discharging process also reduce the cycling life and power density.^[4]

Several sulfur host materials have been proposed to overcome the aforementioned limitations.^[2,5] Carbon-based hosts with high electrical conductivity and large specific surface area (SSA), like graphene,^[6] carbon nanotubes^[7] and hollow carbon spheres,^[8] have been employed to disperse sulfur species and confine the volume expansion. However, the weak physical interaction between LiPS and the non-polar surfaces of these materials makes them ineffective to capture soluble LiPS, which results in a serious shuttle effect and a reduced cyclability.^[9] Previous work has demonstrated that LiPS can be confined through strong chemical binding and rapid catalytic conversion at polar surfaces.^[10] In this direction, the use of transition metal oxides (TMO) and sulfides (TMS) remarkably improve cycling performance. But unfortunately, polar TMO/TMS usually suffer from unsatisfying electrical conductivities that greatly limit the rate performance.

Alternatively, transition metal phosphides (TMP) with metallic character may simultaneously provide the required high electrical conductivity and polar surfaces. [11,12] Besides, TMP also shows exceptional catalytic activity towards Li-S redox reactions. As an example, the Qian group showed cobalt phosphide to exhibit the best catalytic performance among several Co-based compounds and associated this experimental evidence with an appropriate p-band position. [13] To maximize the amount of LiPS adsorption sites and catalytic activity, the TMP should be nanostructured. In this direction, TMP nanocrystals (NCs) can provide high SSAs and abundant unsaturated sites and defects to effectively reduce the reaction energy barrier. [14] To prevent their aggregation caused by the surface energy, and also compensate for the relatively high volumetric density of TMP, TMP NCs can be combined with lightweight support, which should be characterized by a large SSA to support a high dispersion of the TMP phase and high porosity to allow an effective diffusion of lithium ions.

As a proper support material, graphite C₃N₄ is based on abundant elements and it can be obtained with high SSA.^[15] Besides, in contrast to graphene and carbon nanotubes, the presence of Lewis-base pyridine nitrogen in C₃N₄ can effectively interact with the strong Lewis-acid of terminal Li atoms in LiPS, thus contributing to prolonging the lifespan of LSBs.^[16–18] In terms of geometric structure, graphite C₃N₄ nanosheets (s-CN) prepared by the traditional liquid-phase exfoliation method usually suffer from low SSA due to re-aggregation

by Van der Waals forces.^[19] On the other hand, template methods to produce high-SSA C₃N₄ are cumbersome and wasteful, inappropriate for a technology with a huge potential market and thus potentially requiring enormous amounts of materials.^[15]

Besides, the catalytic activity of C₃N₄-based catalysts can be significantly augmented by altering their electronic structures through tuning the surface/interface atom environment. [20,21] When combining metallic TMP NCs with n-type semiconductive C₃N₄, the charge is rearranged at the created Mott-Schottky junction and a built-in electric field appears at the TMP/C₃N₄ interphase. [22,23] This electric field potentially promotes the catalytic activity and subsequently the LSBs performance. To the best of our knowledge, there is no report investigating the electronic structure of TMP/C₃N₄ heterojunctions attempt to apply for LSBs. In the present study, we first engineer and characterize a novel porous graphite C₃N₄ tubular structure (t-CN). Subsequently, we use an electrostatic self-assembly method to blend this novel t-CN with colloidal CoFeP NCs. The obtained tubular CoFeP@CN Mott-Schottky catalysts are then analyzed both experimentally and through theoretical calculations. Afterwards, the performance of S@CoFeP@CN cathodes is thoroughly tested and their superior cycling stability and rate capability are demonstrated. Finally, lithium-sulfur pouch cells are manufactured and their potential toward practical applications is validated.

Results and discussions

t-CN was synthesized by annealing a mixture of urea and melamine that had been previously pressed at 10 MPa. The mixture was annealed at 550 °C during 4 h in air and resulted in a yellow powder (see details in the Experiment Section). No post-exfoliation or etching treatment was carried out. Scanning electron microscopy (SEM) characterization of the yellow powder displayed a hollow tubular structure with 300-500 nm outer diameter and several micrometer long tubes (Figures 1a). Transmission electron microscopy (TEM) confirmed the tubular morphology of the product and further displayed the tube walls to be highly porous (Figures 1b and S1a). Powder X-ray diffraction (XRD) patterns revealed the obtained powder to display the graphite C₃N₄ crystal structure (Figure S1b). The uniform distribution of C and N in t-CN was confirmed by scanning transmission electron microscopy-electron energy loss spectroscopy (STEM-EELS) and X-ray photoelectron spectroscopy (XPS) (Figure S1a,c). Meanwhile, the high-resolution XPS N1s spectrum (Figure S1d) proved a high 68.3% content of pyridinic nitrogen, which could be beneficial to capture LiPS by forming Li-N bonds through its extra pair of electrons.^[16]

As a reference material, graphite C_3N_4 nanosheets (s-CN) were produced through the conventional liquid-phase exfoliation method. XRD and SEM analysis showed s-CN to have a similar crystallinity as t-CN, but an obviously different geometry (Figure S2a,b). The Brunauer–Emmett–Teller (BET) SSA of t-CN was 185.87 m² g⁻¹ and its pore volume 0.85 cm³ g⁻¹. This contrasted with the sevenfold lower SSA and sixfold lower pore volume obtained for s-CN (Figure S2c), related to the different geometry. s-CN suffers from strong Van der Waals' interaction that drives their re-stacking and thus results in moderate surface areas. On the contrary, the folding of C_3N_4 sheets into tubular structures can effectively avoid stacking, thus providing much larger SSAs and pore volumes. A comparison of the SSA and pore volume of previously reported graphite C_3N_4 can be found in Table S1. Besides a simple preparation, the t-CN reported here exhibited significant advantages in terms of SSA and pore volume compared with previously reported materials.

CoFeP NCs with an elongated geometry and an average size of 21.2 ± 3.2 nm were produced using our previously reported colloidal synthesis method (Figure 1c). [24] A uniform

distribution of Co, Fe, and P elements within each particle was revealed by STEM-EELS elemental composition maps (Figure 1d). High-resolution TEM (HRTEM) and XRD characterization proved the CoFeP NCs to have an orthorhombic crystal phase belonging to the *pnma* space group (JCPDS 01-082-5970, Figures 1d and S3). SEM-energy dispersive x-ray spectroscopy (EDX) analysis revealed the ratio of the elements of Co: Fe: P to be close to 1:1:1.2 (Figure S3b), with the small excess of phosphorous most probably located at the NC surface and playing a ligand role.^[25]

Zeta potential measurements (Figure S4) revealed the different signs of the charge at the surface of CoFeP NCs (positively charged) and t-CN (negatively charged). Taking advantage of this different charge, CoFeP@CN nanocomposites with a 1:1 mass ratio were prepared by a simple solution-phase electrostatic self-assembly method (Figure 1e,f).^[26] This process maintained the tubular morphology of t-CN intact (Figure 1g).^[27] EDX elemental maps showed a homogeneous dispersion of CoFeP NCs throughout the t-CN surface (Figure 1h). High-angle annular dark-field (HAADF) images further confirmed the homogeneous distribution of CoFeP NCs on t-CN (Figure 1i). In HAADF images, CoFeP NCs with a higher atomic number possess a stronger ability to scatter electrons than t-CN, thus appear much brighter. XRD patterns of the composites displayed diffraction peaks corresponding to both crystallographic structures: the diffraction peak at 27.4° belonging to the (002) plane of graphite C₃N₄ and the diffraction peaks at 40.5° and 51.7° corresponding to the (112) and (020) planes of CoFeP (Figure 1k).

Graphite C₃N₄ is an n-type semiconductor. Its computed work function (WF) is around 4.4 eV and its band gap is ~2.6 eV.^[28] On the other hand, the WF of metallic CoFeP can be estimated at around 4.8 eV (Figure S5).^[23,29]. When placed in contact, the difference in Fermi levels drives an injection of electrons from C₃N₄ to CoFeP, until the WFs of the two materials at the interface are equilibrated. At equilibrium, an upward bending of the electron energy bands of C₃N₄ at the interface and an electric field pointing from C₃N₄ to CoFeP remain, forming a Mott-Schottky heterostructure (Figure 2a and b).^[23,30]

High-resolution XPS valence band spectra confirmed the semiconducting and metallic character of t-CN and CoFeP, respectively (Figure S6b). The XPS valence band spectrum of

CoFeP@CN composite also showed the Fermi level to lay within a band of states, as in the case of CoFeP. The C 1s spectra of g-CN and CoFeP@CN showed three bands (Figure 2c). The band at 284.8 eV corresponding to adventitious C-C was used as a reference. The main C 1s peak from t-CN was located at 288.47 eV and corresponded to the N-C=N chemical environment of carbon nitride. [31] In the composite material, a significant blue shift of the this N-C=N band, up to 288.69 eV, was obtained. This shift was related to the electron loss of t-CN when in contact with CoFeP NCs. [31,32]

The Co 2p spectrum of CoFeP displayed two bands at 778.58 eV (2p_{3/2}) and 793.42 eV (2p_{1/2}), associated with a Co-P chemical environment (Figure 2d). Two additional bands at 781.60 eV (2p_{3/2}) and 797.47 eV (2p_{1/2}) were assigned to oxidized cobalt species arising from the exposure of the sample to air during handling and transportation.^[22,33] Additional shake-up satellite peaks located at 786.10 eV and 803.20 eV were also discerned. A slight shift of the Co 2p bands toward lower binding energies was observed when supporting the CoFeP NCs on t-CN, consistent with a charge arrangement at the interface and an increased electron density in Co atoms.^[22,33]

Similar results were obtained when analyzing the Fe 2p spectra, displaying bands associated with a Fe-P environment at 707.59eV ($2p_{3/2}$) and 720.04 eV ($2p_{1/2}$), and bands associated to an oxidized environment at 710.74 eV ($2p_{3/2}$) and 724.19 eV ($2p_{1/2}$).^[34] A similar band shift was observed for Fe and Co when contacting CoFeP with t-CN (Figure S6c).

A larger degree of surface oxidation was observed in the CoFeP NCs supported on t-CN than in the unsupported NCs. However, XRD patterns in Figure 1i confirmed the presence of the CoFeP phase in both samples, indicating an overall low content of CoPO_x or FePO_x in CoFeP@CN samples. Notice in any case that recent reports have demonstrated that TMPs with an oxidized surface can still effectively promote LiPS capture through the metal oxide and phosphate sites, which can form strong metal—S and oxide P–Li bonds, respectively.^[35]

Density functional theory (DFT) calculations further demonstrated a charge redistribution at the atomic scale when placing the two materials in contact. According to XRD results of CoFeP, we constructed a slab model based on the exposed CoFeP (112) facet and a graphite C₃N₄ monolayer to evaluate the charge transfer at the interface. Bader charge analysis

calculated charge redistribution at the CoFeP/C₃N₄ interface and quantified that the bottom CoFeP unit cell gains 1.84 electrons from the CN layer. The gain/loss of electrons of the different atoms is displayed in Figure 2e.

Sulfur was introduced within the CoFeP@CN by a melt-diffusion process (see the Experimental Section for details). SEM characterization of the obtained S@CoFeP@CN composites revealed the tubular structure of CoFeP@CN to be conserved after S addition (Figure S7a). XRD patterns confirmed the presence of crystalline sulfur (JCPDS No. 08-0247) within S@CoFeP@CN composites (Figure S7b)[36] and a homogenous distribution of the different elements was proven by EDS mapping (Figure S7c). With the introduction of sulfur, the SSA value sharply decreased from 86.8 m² g⁻¹ (CoFeP@CN) to 1.8 m² g⁻¹ (S@CoFeP@CN), as shown in Figure S7d. Thermogravimetric analysis (TGA) allowed quantifying the sulfur content in the S@CoFeP@CN composite at about 70 wt%, consistent with the nominal amount introduced (Figure S7e). The same preparation process was employed to load equivalent amounts of sulfur into other hosts, CoFeP, t-CN, and Super P, which were used as reference materials when testing CoFeP@CN performance (Figure S8).

The LiPS adsorption ability of the host material plays a key role in suppressing the shuttle effect in LSBs, thus it is the first property analyzed when screening different materials toward finding a good sulfur host. To evaluate LiPS affinity, the same amount of the different hosts was immersed into a 10 mM LiPS (~Li₂S₆) solution. After 12 h, clear differences in the color of the solution containing the different materials were observed, indicating a different degree of LiPS adsorption (Figures 3a,S9). Adsorption results were also confirmed by analyzing the UV–vis spectra of the solutions in the range of 400-500 cm⁻¹ (Figure 3b).^[37–39]

Comparing the t-CN developed here with s-CN obtained by conventional exfoliation methods, we observed how the t-CN exhibited a much higher LiPS adsorption ability as qualitatively observed by the much lighter color of its final solution (Figures S9). This result is consistent with the larger SSA and pore volume of t-CN compared with s-CN. Subsequently, we compared the LiPS adsorption ability of CofeP@CN, CoFeP, t-CN, and Super P. We noticed that the color of the solutions containing t-CN and/or CoFeP was much lighter than that of the solution containing Super P, inferring a stronger interaction of t-CN and CoFeP with LiPS.

The clearest solution was obtained with the presence of CoFeP@CN, demonstrating that the composite was characterized by an additional LiPS adsorption capability when compared with the same amount of each of the components.

Additional XPS analyses were conducted to understand the chemical interaction between CoFeP@CN and LiPS during the Li₂S₆ adsorption experiment. From the comparison of the N 1s spectra of the composite before and after Li₂S₆ adsorption (Figure 3c), a distinct shift could be observed in the pyridinic-N band from 399.08 eV to 399.25 eV.^[40] The small additional band in the CoFeP@CN-LiPS sample at 397.75 eV is attributed to N-Li bond formation during the adsorption process.^[41,42] These results were consistent with previous reports demonstrating that LiPS could anchor on active nitrogen sites through dipole-dipole interactions. This Li–N chemical interaction certainly contributes to inhibiting the shuttling effect.^[43]

Meanwhile, the Co 2p_{3/2} and Fe 2p_{3/2} XPS spectra displayed in Figure 3d,e show that after interaction with Li₂S₆, bands corresponding to Co–P or Fe–P environments suffered an obvious shift to higher binding energy, indicating the formation of Co–P/S and Fe–P/S bonds.^[37,44] Additionally, the relative intensity of the oxide Co and Fe bands decreased in the CoFeP@CN-LiPS sample, which was also consistent with the formation of strong Co-S and Fe-S bonds during the Li₂S₆ adsorption process which partially prevented the surface oxidation.^[35,37] In Figure 3f, a band shift can be also found in the P 2p spectrum, which might be attributed to the accumulation of electrons at P sites related to the interaction with terminal Li atoms in Li₂S₆ species.^[45,46]

DFT calculations were conducted to determine the affinity between chained LiPS species and CoFeP and t-CN. The binding energies and atomic structures between LiPS (Li₂S₂, Li₂S₄, Li₂S₆, and Li₂S₈) and CoFeP (001) and graphite C₃N₄ (001) surfaces were calculated (Figure S10). Compared with previous reports on graphitic carbon, [47,48] the more negative LiPS binding energies on the surface of CoFeP and graphite C₃N₄ (Figure 3i) indicated stronger adsorption of soluble LiPS on the latter two. The chemical adsorption of LiPS with CoFeP@CN is mainly originated from the treble interactions: i) Lewis-base pyridine N in t-CN with extra pair of electrons interact with Lewis acid of terminal Li^{δ+} atoms in LiPS; ii)

chemical bonding between the terminal S^{δ^-} atoms and $Co^{\delta^+}/Fe^{\delta^+}$ atoms in CoFeP NCs; and iii) chemical bonding between Li^{δ^+} atoms and P^{δ^-} atoms. Taking Li_2S_6 -adsorbed structures as an example (Figure 3 g and h), Li atoms preferentially bind to N sites in C_3N_4 , with a Li-N bond distance in the C_3N_4/Li_2S_6 model of only 2.10 Å. S atoms tend to bind with Co and Fe atoms into a small 2.16 Å Co-S and 2.21 Å Fe-S bond distance. Besides, the calculated Li-P bond distance was 2.50 Å. Overall, the coexistence of multiple adsorption sites to strongly capture the LiPS by Li-N, Fe/Co-S and Li-P bonds endow the great potential of CoFeP@CN composite as S host in LSBs.

To evaluate the ability of host materials to catalytically accelerate the kinetics of polysulfide conversion, cyclic voltammetry (CV) tests of Li₂S₆ symmetrical cells were conducted in the voltage window -1 to 1 V. As shown in Figure 4a, t-CN, CoFeP, and CoFeP@CN electrodes showed significantly different CV curves. The symmetric curves of CoFeP@CN electrodes exhibited higher peak current densities than t-CN and CoFeP electrodes, demonstrating the combination of both materials within a heterostructured composite to boost the electrochemical activity of polysulfide conversion.^[49] When similar experiments were carried out on CoFeP@CN electrodes without Li₂S₆ addition in the electrolyte (Figure S11), the approximately rectangular-shaped CV curves obtained demonstrated a pure capacitive behavior rather than a chemical reaction. This result implies that Li₂S₆ was the unique electrochemically active species in the system.^[36]

The electrochemical performance of the electrodes was evaluated using LSBs assembled in coin cells. Figure 4b displays the CV curves obtained from S@t-CN, S@CoFeP, and S@CoFeP@CN cells. All curves showed two reduction peaks (peak I and II), which corresponded to a two-step S reduction process upon cathodic scanning: peak I was attributed to the transformation from S_8 to soluble long-chain LiPSs (Li₂S_x, $4 \le x \le 8$), followed by a further reduction to insoluble Li₂S₂/Li₂S in peak II. [48,50] The anodic peak (peak III) was ascribed to the reverse multistep oxidation process of short-chain sulfides to LiPS and eventually to sulfur. S@CoFeP@CN electrodes exhibited the most intense peak currents and the cathodic/anodic peaks located at the most positive/negative potentials (Figure 4c). This result indicated that among the tested materials, CoFeP@CN was the most effective catalyst

in promoting the polysulfides redox reaction kinetics. Catalytic activities were further quantified through the onset potentials at $10~\mu A~cm^{-2}$ current density beyond the baseline current (Figure S12). Among the three kinds of electrode tested, the onset potentials of S@CoFeP@CN were the highest/lowest in reduction/oxidation peaks (Figure 4c), demonstrating an effective decrease of the overpotential in LiPS conversion reaction.

Charging/discharging tests at different current rates were conducted for the three types of electrodes. At the current rate of 0.1 C, all electrodes showed one charging and two discharging plateaus, consistently with the measured CV peaks (Figure 4d). A voltage gap ΔE found between the oxidation and the second reduction plateaus introduced polarization potential in the redox reaction, which was taken as the voltage gap at 50% discharged capacity. S@CoFeP@CN electrodes displayed a lower polarization potential ($\Delta E = 147$ mV) than S@CoFeP ($\Delta E = 158$ mV) and S@t-CN electrodes ($\Delta E = 211$ mV), demonstrating the synergism between the two components within CoFeP@CN to accelerate the LiPS conversion kinetics. S@CoFeP electrodes exhibited a much better polarization than S@CN because of the intrinsic metallic and semiconductor nature of CoFeP and t-CN, respectively. S@CoFeP@CN electrodes also exhibited the lowest overpotentials in the phase conversion between soluble Li₂S₄ and insoluble Li₂S₂/Li₂S (Figure S13). [52]

The catalytic activity of the host materials toward the LiPS conversion reaction can be quantified by the ratio Q2/Q1, where Q1 and Q2 denote the capacity of the two discharge plateaus (Figure 4d). Q1 corresponds to the reduction of sulfur to soluble LiPS (S_8 + $4Li^+$ + $4e^- \rightarrow 2Li_2S_4$) and Q2 to the subsequent transfer to insoluble sulfide ($2Li_2S_4$ + $12Li^+$ + $12e^- \rightarrow 8Li_2S$), respectively. During the second plateau (Q2), the final product Li₂S generally accompanied by the presence of Li₂S₂ due to sluggish reaction kinetics, which inhibits the release of capacity during the Q2 stages. Thus, while the capacity ratio should be Q2/Q1 = 3, taking into account the electrons involved in each process (4 for Q1 and 12 for Q2), generally ratios lower than 3 are obtained. Additionally, the LiPS shuttle effect is also reflected in a capacity loss. In all cases, the higher Q2/Q1, the better the catalytic ability. As displayed in Figure 4e, S@CoFeP@CN exhibited the highest Q2/Q1 ratio at 2.74, close to the theoretical value and well above that of S@CoFeP (2.47) and S@t-CN (2.17), which further evidenced

the synergistic effect towards LiPS redox reaction obtained when combining both materials in the CoFeP@CN Mott-Schottky heterostructure.

The efficiency of LSBs is limited by the high charging/discharging overpotentials that are in large part related to the sluggish kinetics of deposition/dissolution of insulating solid Li₂S.^{[53][54]} Thus, we performed Li₂S nucleation and dissolution experiments to further assess the performance of the materials developed here. For this experiment, electrode materials were supported on carbon paper (CP, see details in the Supporting Information) which is able to soak the catholyte. From the potentiostatic discharge profiles in Figure 4g, CP/CoFeP@CN exhibited the sharpest nucleation peak and the fastest responsivity toward Li₂S nucleation, when compared with CP/t-CN and CP/CoFeP electrodes. According to Faraday's law, the conversion capacity was obtained by integrating the area below the current curves. The Li₂S deposition capacity of CP/CoFeP@CN (237.9 mAh g⁻¹) was larger than that of CP/t-CN and CP/CoFeP electrodes (141.5 mAh g⁻¹ and 165.4 mAh g⁻¹, respectively), demonstrating that CoFeP@CN could effectively decrease the overpotential and promote the Li₂S nucleation reaction. [36,54] We investigated the kinetics of the Li₂S dissolution experiment using a similar protocol (Figure S14). In the potentiostatic charge curves, the highest peak current densities and shortest peak current time were obtained for the CP/CoFeP@CN electrode, indicating a faster Li₂S dissolution. Moreover, CP/CoFeP@CN electrodes revealed a 532 mAh g⁻¹ dissolution capacity, much higher than that measured for the other electrodes (406 mAh g⁻¹ for CP/t-CN and 466 mAh g⁻¹ for CP/CoFeP).

To further verify the catalytic activity of catalysts on the LiPS conversion, the Gibbs free energy changes during the LiPS reduction on t-CN, CoFeP, and CoFeP@CN were calculated (Figure 4h). For the liquid-to-solid (Li₂S₆ to Li₂S) nucleation reaction, all LiPS reduction steps were endothermic with relatively large positive Gibbs energy barriers, especially for the Li₂S₂ to Li₂S conversion, which was the rate-limiting step.^[55] However, CoFeP@CN exhibited the lowest Gibbs free energy changes (0.47 eV) than CoFeP and t-CN (0.61 and 0.75 eV, respectively), and this value is much lower than previously reported graphene or N-doped graphene (above 1 eV), which suggested that the composite CoFeP@CN was a relatively excellent catalyst to promote the LiPS conversion kinetics.^[52,56,57] The lowest Gibbs

free energy change in the reduction of Li₂S₂ measured for CoFeP@CN was consisted of Li₂S nucleation test and overall, these results demonstrated that CoFeP@CN Mott-Schottky heterostructure catalyst plays a catalytic role to accelerate the Li₂S formation.

To obtain further insight into the role of CoFeP@CN in accelerating the LiPS reaction, electrode kinetics were further analyzed by measuring CV at different scan rates, from 0.1 to 0.4 mV s⁻¹ (Figure 4f). When increasing the scan rate, the two cathodic peaks shifted to more negative potentials and the anodic peak shifted to a positive potential, overall increasing the polarization voltage. The linear relationship between the anodic/cathodic peak current and the square root of the scanning rates pointed at a diffusion-limited reaction (insert in Figure 4f). Thus, the classical Randles–Sevcik equation was used to calculate the Li⁺ diffusivity in the process:^[58,59]

$$I_{p} = (2.69 \cdot 10^{5}) n^{1.5} A D_{L_{i}+}^{0.5} C_{L_{i}+} v^{0.5}$$
(1)

where I_p is the peak current, n is the number of charge transfer, A is the geometric electrode area, D_{Li^+} is the Li⁺ diffusion coefficient, C_{Li^+} is the concentration of Li⁺ in the electrolyte, and v is the scan rate. At a given n, A, and C_{Li^+} , sharper $Ip/v^{0.5}$ slopes denote faster Li⁺ diffusion. As displayed in Figures 4f,i and S15, S@CoFeP@CN electrodes exhibited the sharpest slopes for the 3 peaks, thus the highest Li⁺ diffusivity during the redox reactions. In peak I, II and III, the Li⁺ diffusion coefficients of S@CoFeP@CN were 2.15, 3.92, and 5.26×10^{-7} cm² S⁻¹, respectively. Li⁺ diffusivity strongly depends on the viscosity of the electrolyte containing LiPS and the accumulation of insulating Li₂S/Li₂S₂ on the electrode. [36,59] The highest diffusivities obtained for the CoFeP@CN host reflected that the improved reaction kinetics was in part related to a confined shuttle effect and an improved catalytic activity towards LiPS conversion, consistently with the above results.

Figure 5a shows the rate performances of the three types of electrodes tested, at current rates from 0.1 to 5 C. S@CoFeP@CN electrodes systematically exhibited the highest discharge capacity at any current rate among the different electrodes tested. A high initial discharge capacity at 1607 mAh g⁻¹ was measured, demonstrating a very high sulfur activity and utilization. Even at high current rates of 5 C, the average capacity stabilized at 630 mAh g⁻¹,

well above the capacity obtained for S@CoFeP and S@CN electrodes, 406 mAh g⁻¹ and 0.23 mAh g⁻¹, respectively. When the current rate was returned to 0.2 C, the average capacity of the cells with S@CoFeP@CN electrodes returned to approximately 1010 mAh g⁻¹, demonstrating remarkable reversibility and stability. It is worth mentioning that a negligible capacity was obtained from pure CoFeP@CN electrodes, *i.e.* without sulfur, under the same measuring conditions (Figure S16). The galvanostatic charging/discharging profiles of S@CoFeP@CN at different current rates are displayed in Figure 5b. All discharge curves exhibited two well-defined discharge plateaus, even at a current density of 5 C. In contrast, S@CoFeP electrodes displayed a similar shape but much lower capacity (Figure S17a), and S@CN electrodes showed a high polarization potential and no capacity response above 2 C (Figure S17b), due to the huge potential barrier and the limited conductivity of the electrode material.

To evaluate the long-term cycling stability of the different host materials, cells were continuously cycled at 1 C (Figure 5c). The initial discharge capacity of S@CoFeP@CN electrodes at 1 C was about 844 mAh g⁻¹, and retained about 96.5 % capacity, 814 mAh g⁻¹, after 200 cycles. Significantly lower capacity retention was obtained for S@CoFeP electrodes (81.4%), which suffered a notable capacity decay during the first 100 cycles. This result might be attributed to the relatively low SSA (38 m² g⁻¹ by BET) of the nanocrystalline CoFeP host which had insufficient active sites to anchor the initial excess of sulfur species, but as the S content decreased, its stability improved owing to its sulfiphilic surface. Surprisingly, even though S@t-CN electrodes exhibited a relatively low initial capacity, they were characterized by remarkable stabilities, with retention of about 96.6% after 200 cycles. This superior stability can be explained by the t-CN with tubular structure here presented that provides a very high SSA to trap LiPS species by the lithiophilic sites and a high pore volume to accommodate the volume change during cycles. Additional cycling was carried out on the S@CoFeP@CN electrodes at a higher current rate of 3 C (Figure 6d). After 700 cycles at 3 C, S@CoFeP@CN electrodes still provided a discharge capacity of 606 mAh g⁻¹, showing an average 0.014% decay per cycle and a stable and high coulombic efficiency above 99.6%.

The LSB energy conversion efficiency in the charging/discharging process, different from the

above coulombic efficiency, was calculated by the ratio of energy output/input (E = $\int UIdt$). [48,60] At 0.1 C current rate, the three types of electrode tested exhibited a high energy efficiency of around 90% (Figure 5e). When increasing the current rate, S@CoFeP@CN displayed the highest and most stable energy efficiency, retaining 89.91% efficiency at 1 C and 79.89% at 5 C, well above the 69.37% for S@CN at 1 C and 74.61% for S@CoFeP at 5 C. We associate this higher energy efficiency to the lower polarization potential of CoFeP@CN electrodes, which was in turn related to its excellent catalytic properties, as discussed above.

Self-discharging is another main drawback of LSBs. The self-discharge profiles of S@CoFeP@CN and S@Super P electrodes are presented in Figure 5f. The open-circuit voltage (OCV) of the cells was measured during 72 consecutive hours after 30 stabilization cycles. During this time, S@Super P electrodes showed a significant OCV decrease to 2.288 V, denoting a notable self-discharging. On the other hand, the S@CoFeP@CN electrode maintained a much more stable OCV, with a final voltage of 2.367 V, suggesting superior stability against self-discharge. Self-discharging may be more clearly seen in the right side of Figure 5f, where the dash/solid curves present the discharge curves before/after 72 h of rest under a current rate of 0.2 C. After the 72 h rest period, an obvious capacity decay, from 691 to 580 mAh g⁻¹, was obtained from the S@Super P electrode, consistently with the OCV change. On the other hand, just a slight capacity loss was measured from the S@CoFeP@CN electrode, from 989.2 to 975.5 mAh g⁻¹. Under shelf storage conditions, the capacity of batteries shows exponential decay with storage time t_S, so the self-discharge behavior can be quantitatively analyzed using the following equation:^[61]

$$Q_D = Q_D^0 e^{-K_S t_S}$$
 (2)

 Q_D^0 and Q_D are discharge capacity before and after storage for a period of time t_S , so the self-discharge constant K_S can be easily obtained from:

$$K_S = \ln \frac{Q_D^0}{Q_D} \cdot \frac{1}{\mathsf{t}_S} \tag{3}$$

While S@Super P electrodes were characterized by a K_S value of $2.40 \times 10^{-3} \text{ h}^{-1}$, an order of

magnitude lower self-discharge constant was obtained for S@CoFeP@CN, $K_S = 1.96 \times 10^{-4}$ h⁻¹. The lower self-discharge constant of S@CoFeP@CN batteries was related to the lower loss of active material and a stronger LiPS anchoring.

Electrochemical impedance spectroscopy (EIS) was used to further understand the parameters behind the enhanced redox kinetics of S@CoFeP@CN electrodes. Figures 5g and S18 display the Nyquist plot obtained from S@CoFeP@CN, S@CoFeP, and S@CN coin cells before and after cycling at 1 C. The fresh electrodes displayed a semicircle in the high-frequency region associated with the charge-transfer resistance (Rct), followed by a linear dependence in the low-frequency region that is related to the diffusion of lithium ions.^[36,62] Data was fitted considering the equivalent circuit displayed as an inset in Figure 6g. A moderate Rct was obtained for the S@CoFeP@CN electrode (62.99 Ω), when compared with that of S@CoFeP (80.36Ω) and S@CN (125.5 Ω). This low Rct denoted an enhanced charge transferability of the CoFeP@CN composite when compared with electrodes based on each of the composite components. After charging/discharging loops, an additional semicircle in the high-frequency range was evidenced. This newly appearing loop was associated with the resistance of an insoluble Li₂S₂/Li₂S passivation layer (Rp in the equivalent circuit) grown during cycling. [55,62] After cycling, Rct notably decreased for the three types of electrode tested due to the activation process. After cycling, S@CoFeP@CN electrodes were characterized by smaller Rct (9.56 Ω) and Rp (20.14 Ω), when compared with S@CoFeP (Rct = 29.39 Ω and Rp = 23.36 Ω) and S@CN electrodes (Rct = 52.67 Ω and Rp = 120.91 Ω). The small Rp value obtained for CoFeP and specially CoFeP@CN hosts indicated a reduction of the deposition of insulting Li₂S/Li₂S₂ on the surface, associated with an accelerated LiPS conversion.^[62]

To thoroughly demonstrate that CoFeP@CN host could effectively capture soluble LiPS to confine the shuttle effect in the charging/discharging process, cycled coin cells were disassembled and analyzed. A striking contrast in the color of separators of the different cells can be observed in Figure 5h. The membrane disassembled from a S@CoFeP@CN cell (left one) showed a much lighter color than the dark brown membrane recovered from a S@Super P (right one). This simple visual inspection demonstrated that the CoFeP@CN host could trap polysulfide much more effectively than Super P, and thus suppressed self-discharging and

overall improved the cell efficiency and stability. Another strong evidence in support of the inhibited LiPS dissolution of CoFeP@CN was found from the surface morphology of the cycled Li anode. Different from the large cracks and severe corrosion phenomenon observed in the surface of the Li anodes recovered from S@Super P coin cells, Li foils recovered from cycled S@CoFeP@CN coin cells showed a smooth surface and lower sulfur signal at their surface, as detected by SEM and EDS analysis (Figure 5j,k). Finally, Figure 5i displays the morphology of cycled S@CoFeP@CN. Due to the inevitable grinding and shearing treatment during the slurry preparation, partial crushing happened on the S@CoFeP@CN composite, but the original tubular nanostructure was still recognizable after cycling, indicating good mechanical stability of the material towards lithiation/delithiation cycles.

Increasing the sulfur loading is mandatory to achieve the high energy density LSBs required in practical applications. Hence, a series of electrochemical tests of S@CoFeP@CN electrodes were conducted at 4.1 mg cm⁻² sulfur loading. The results of the rate performance of cells produced with such high S loading can be found in Figure 6a and S19. S@CoFeP@CN electrodes displayed high initial discharge capacities at 1255 mAh g⁻¹, which corresponded to an areal capacity of 5.15 mAh cm⁻², notably above that of commercial LIBs (4 mAh cm⁻²). Even at high current rates of 3 C, a stable discharge capacity at 508 mAh g⁻¹ was obtained. Besides, when the current rate was returned to 0.2 C, the initial capacity was recovered (Figure S19). All the galvanostatic charging/discharging profiles at different current rates clearly exhibited one charge plateau and two discharge plateaus, indicating that CoFeP@CN hosts could effectively reduce the polarization of LiPS conversion even under high sulfur-loading (Figure 6a). Figure 6b shows the long-term cycling performance of high sulfur loading S@CoFeP@CN electrode at 1 C. After 400 cycles, the discharge capacity was maintained at 608 mAh g⁻¹, which involved an 87.6% capacity retention, i.e. a 0.031% average capacity loss per cycle. S@CoFeP@CN electrodes were also characterized by a high and stable coulombic efficiency at 99.3%. Table S2 displays a comparison of several parameters of state-of-the-art TMP-based and C₃N₄-based materials as cathode hosts for LSBs. Notice that the CoFeP@CN host presented here is characterized by the highest capacities and stabilities. Besides, to illustrate the practical applicability of LSBs based on S@CoFeP@CN

cathodes, pouch cells were also fabricated according to the schematic diagram shown in Figure S 20. S@CoFeP@CN-based pouch batteries revealed good stability at 0.4 C during 200 cycles, remarkable capacity retention of 89.6% was obtained and accompanied by a high coulombic efficiency at 99.5% (Figure 6d), and the charged mobile phone clearly demonstrate their potential (Figure 6c, Video S1). All these results indicate that S@CoFeP@CN electrodes can definitively help LSBs to reach practical applications.

Conclusion

In summary, we reported a highly efficient sulfur host for robust LSBs, enabled by orthorhombic phased bimetallic phosphide CoFeP NCs decorated on novel nanotubular t-CN by a facile self-assembly process that took advantage of the different sign of the particles surface charge. While each of the materials provided advantages in terms of adsorption sites and available SSA, the combination of the two materials within CoFeP@CN heterostructures awoke a clear synergism between them that significantly contributed to improving LiPS adsorption and catalytic activity. Besides t-CN allowing a high distribution of CoFeP NCs, experimental results and DFT calculations displayed a charge redistribution within the formed Mott-Schottky heterostructures. Additionally, experimental and theoretical work also confirmed the superior LiPS adsorbability realized by abundant sulfiphilic/lithiophilic sites in CoFeP and t-CN. Besides, the modified electron distribution within heterostructures allowed reducing the potential barriers and improved the redox kinetics during charging/discharging processes, including LiPS phase change and Li₂S deposition/dissolution. Moreover, the porous CoFeP@CN host provides sufficient space to accommodate the volume change and efficient channels for Li⁺ diffusion in reaction. As a result, S@CoFeP@CN electrodes delivered a high sulfur utilization, superior rate performance (630 mAh g⁻¹ at 5 C), and remarkable cycling stability with 90.44% capacity retention over 700 cycles at 3 C. Even with 4.1 mg cm⁻² high-loading sulfur electrode coin cells and the 0.1 Ah capacity pouch cells test, the robust electrochemical performance results were obtained. In addition, S@CoFeP@CN electrodes exhibit high energy efficiency and low self-discharge property, which are two frequently neglected issues in material research of LSBs. This work not only demonstrated a new and highly suitable form of t-CN and further probed the suitability of metal phosphides in the field of LSBs, but also provided valuable insights into the design of heterostructural electrocatalyst to regulate LiPS.

Experiment section

Preparing of CoFeP nanoparticles. In a typical synthesis, 2.4 g (10 mmol) of 1-hexadecylamine (HDA, 90%, Acros Organics) were combined with 10.0 mL of 1-octadecene (ODE, 90%, ACROS Organics) and 2.6 mL (10 mmol) of triphenyl phosphite (TPP, 99%, ACROS Organics) in a 50 mL flask. The system was degassed and heated to 150 °C and maintained at this temperature for 1 h to remove low boiling point impurities, moisture, and oxygen. After 4 mL ODE contain 384 mg (1 mmol) Co₂(CO)₈ (95%, ACROS Organics) and 390 mg (2 mmol) Fe(CO)₅ (Sigma-Aldrich) was added into the system the temperature was then increased to 290 °C in 20 min and kept there for 1 h. Afterward, the mixture was allowed to cool down to 200 °C by removing the heating mantle and then cooled rapidly down to room temperature with a water bath. The black product was isolated by precipitation with acetone. To remove as many organics as possible, two redispersion and precipitation cycles using chloroform and acetone were additionally carried out. In the ligand remove the process of CoFeP nanoparticles, 10 mL of CoFeP NPs dispersion (10 mg mL⁻¹) in hexane (99.0%, Honeywell) was combined with 10mL acetonitrile (99%, ACROS Organics) to form a two-phase mixture and then add 1 mL HBF₄ solution (48%) in it. The resulting solution was sonicated until the NCs transferred from the upper to the bottom layer. The surface-modified NCs were washed with ethanol three times and dispersed in 10 mL ethanol with a little amount of N,N-Dimethylformamide (DMF, 99.8%, Alfa Aesa) for further use.

Preparing tubular t-CN. The t-CN was prepared by an annealing method using a mixture of urea and melamine as the precursor. Typically, 100 mg urea (99.5%, ACROS Organics) and 10 mg melamine (99%, ACROS Organics) was put in a mortar and grinded for 10 min. The mixture powder was loaded into a graphite die and compacted into cylinders (Ø 10 mm×10 mm) under a pressure of 10 MPa. Then cylinders were put into a crucible covered loosely with a lid and then heated at 550 °C for 4 h in static air in a muffle furnace. The ramping rate

was 5 °C min⁻¹. After cooled naturally to room temperature, the resultant yellow solid was collected and grounded into powder for further use.

Synthesis of CoFeP@CN composites. 50 mg of t-CN powder was dispersed in 15 mL ethanol and DMF mixed solution and then sonicated for 1 h. Then 5 mL of a CoFeP ethanol dispersion (10 mg mL⁻¹) was added into the mixture solution and stirred for 24 h. The product was washed with ethanol 3 times and dry under vacuum overnight.

Synthesis of S@CN, S@CoFeP, S@CoFeP@CN, and S@Super P. Typically, CoFeP@CN and sulfur powder (99.98%, Sigma Aldrich) were well mixed with the weight ratio of 1:3, and then heated the mixture at 155 °C for 6 h in a sealed glass bottle under Ar protection. The redundant sulfur not incorporated into CoFeP@CN was removed by 10 mL CS₂ (99.9%, Alfa Aesa) and ethanol solution (1:4, volume ratio). S@CN, S@CoFeP, and S@Super P were prepared by the same method.

Acknowledgements

This work was supported by the European Regional Development Funds and by the Spanish Ministerio de Economía y Competitividad through the project ENE2016- 77798-C4-3-R, and ENE2017-85087-C3. C. Zhang, R. Du, K. Xiao D. Yang T. Zhang and X. Wang thank the China Scholarship Council for the scholarship support. Authors acknowledge funding from Generalitat de Catalunya 2017 SGR 327 and 2017 SGR 1246. ICN2 acknowledges the support from the Severo Ochoa Programme (MINECO, grant no. SEV-2017-0706) and is funded by the CERCA Programme/Generalitat de Catalunya. J. Llorca is a Serra Húnter Fellow and is grateful to MICINN/FEDER RTI2018-093996-B-C31, GC 2017 SGR 128 and to ICREA Academia program.

References

- [1] P. G. Bruce, S. A. Freunberger, L. J. Hardwick, J.-M. Tarascon, Nat. Mater. 2012, 11, 19.
- [2] L. Zhou, D. L. Danilov, R. Eichel, P. H. L. Notten, Adv. Energy Mater. 2020, 2001304.
- [3] M. Zhang, W. Chen, L. Xue, Y. Jiao, T. Lei, J. Chu, J. Huang, C. Gong, C. Yan, Y. Yan, Y. Hu, X. Wang, J. Xiong, *Adv. Energy Mater.* **2020**, *10*, 1903008.
- [4] W. Lim, S. Kim, C. Jo, J. Lee, Angew. Chem. Int. Ed. 2019, 58, 18746.
- [5] Z. Li, H. B. Wu, X. W. (David) Lou, Energy Environ. Sci. 2016, 9, 3061.
- [6] C. Zu, A. Manthiram, *Adv. Energy Mater.* **2013**, *3*, 1008.
- [7] J.-Q. Huang, Q. Zhang, S.-M. Zhang, X.-F. Liu, W. Zhu, W.-Z. Qian, F. Wei, *Carbon* **2013**, *58*, 99.
- [8] B. Zhang, X. Qin, G. R. Li, X. P. Gao, Energy Environ. Sci. 2010, 3, 1531.
- [9] H. Wang, W. Zhang, J. Xu, Z. Guo, Adv. Funct. Mater. 2018, 28, 1707520.
- [10] X. Liu, J.-Q. Huang, Q. Zhang, L. Mai, Adv. Mater. 2017, 29, 1601759.
- [11] S. Yu, W. Cai, L. Chen, L. Song, Y. Song, *J. Energy Chem.* **2020**.
- [12] H. Yuan, X. Chen, G. Zhou, W. Zhang, J. Luo, H. Huang, Y. Gan, C. Liang, Y. Xia, J. Zhang, J. Wang, X. Tao, *ACS Energy Lett.* **2017**, *2*, 1711.
- [13] J. Zhou, X. Liu, L. Zhu, J. Zhou, Y. Guan, L. Chen, S. Niu, J. Cai, D. Sun, Y. Zhu, J. Du, G. Wang, Y. Qian, *Joule* **2018**.
- [14] Y. Li, Z. Dong, L. Jiao, Adv. Energy Mater. 2020, 10, 1902104.
- [15] W.-J. Ong, L.-L. Tan, Y. H. Ng, S.-T. Yong, S.-P. Chai, *Chem. Rev.* **2016**, *116*, 7159.
- [16] T.-Z. Hou, X. Chen, H.-J. Peng, J.-Q. Huang, B.-Q. Li, Q. Zhang, B. Li, *Small* **2016**, *12*, 3283.
- [17] Q. Pang, L. F. Nazar, ACS Nano 2016, 10, 4111.
- [18] Z. Jia, H. Zhang, Y. Yu, Y. Chen, J. Yan, X. Li, H. Zhang, *J. Energy Chem.* **2020**, *43*, 71.
- [19] P. Zhang, F. Wang, Y. Qin, N. Wang, ACS Appl. Nano Mater. 2020.
- [20] Y. Wang, R. Zhang, J. Chen, H. Wu, S. Lu, K. Wang, H. Li, C. J. Harris, K. Xi, R. V.

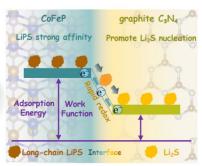
- Kumar, S. Ding, Adv. Energy Mater. 2019, 9, 1900953.
- [21] X. Du, J. Huang, J. Zhang, Y. Yan, C. Wu, Y. Hu, C. Yan, T. Lei, W. Chen, C. Fan, J. Xiong, *Angew. Chem. Int. Ed.* **2019**, *58*, 4484.
- [22] X. Wang, X. Tian, Y. Sun, J. Zhu, F. Li, H. Mu, J. Zhao, *Nanoscale* **2018**, *10*, 12315.
- [23] Z. Zhuang, Y. Li, Z. Li, F. Lv, Z. Lang, K. Zhao, L. Zhou, L. Moskaleva, S. Guo, L. Mai, *Angew. Chem.* **2018**, *130*, 505.
- [24] J. Liu, M. Meyns, T. Zhang, J. Arbiol, A. Cabot, A. Shavel, *Chem. Mater.* **2018**, *30*, 1799.
- [25] J. Liu, X. Yu, R. Du, C. Zhang, T. Zhang, J. Llorca, J. Arbiol, Y. Wang, M. Meyns, A. Cabot, *Appl. Catal. B Environ.* **2019**, *256*, 117846.
- [26] T. Berestok, P. Guardia, M. Ibáñez, M. Meyns, M. Colombo, M. V. Kovalenko, F. Peiró, A. Cabot, *Langmuir* **2018**, *34*, 9167.
- [27] D. Zeng, W. Xu, W.-J. Ong, J. Xu, H. Ren, Y. Chen, H. Zheng, D.-L. Peng, *Appl. Catal. B Environ.* **2018**, *221*, 47.
- [28] Y.-L. Wang, Y. Tian, Z.-L. Lang, W. Guan, L.-K. Yan, *J. Mater. Chem. A* **2018**, *6*, 21056.
- [29] Q. Pang, X. Liang, C. Y. Kwok, J. Kulisch, L. F. Nazar, *Adv. Energy Mater.* **2017**, *7*, 1601630.
- [30] Z. Chen, Y. Yu, X. She, K. Xia, Z. Mo, H. Chen, Y. Song, J. Huang, H. Li, H. Xu, *Appl. Surf. Sci.* **2019**, *495*, 143528.
- [31] Q. Zhu, B. Qiu, H. Duan, Y. Gong, Z. Qin, B. Shen, M. Xing, J. Zhang, *Appl. Catal. B Environ.* **2019**, *259*, 118078.
- [32] J. Wu, C. Li, W. Zhang, J. Han, L. Wang, S. Wang, Y. Wang, *Energy Technol.* **2019**, *7*, 1800927.
- [33] J.-X. Feng, S.-Y. Tong, Y.-X. Tong, G.-R. Li, J. Am. Chem. Soc. **2018**, 140, 5118.
- [34] Z. Peng, X. Qiu, G. Cai, X. Zhang, Z. Dong, J. Alloys Compd. **2020**, 842, 155784.
- [35] Y. Zhong, L. Yin, P. He, W. Liu, Z. Wu, H. Wang, J. Am. Chem. Soc. 2018, 140, 1455.
- [36] C. Zhang, J. J. Biendicho, T. Zhang, R. Du, J. Li, X. Yang, J. Arbiol, Y. Zhou, J. R. Morante, A. Cabot, *Adv. Funct. Mater.* **2019**, *29*, 1903842.

- [37] Y. Chen, W. Zhang, D. Zhou, H. Tian, D. Su, C. Wang, D. Stockdale, F. Kang, B. Li, G. Wang, *ACS Nano* **2019**, *13*, 4731.
- [38] Y. Zhang, Y. Wang, R. Luo, Y. Yang, Y. Lu, Y. Guo, X. Liu, S. Cao, J.-K. Kim, Y. Luo, *Nanoscale Horiz.* **2020**, *5*, 530.
- [39] X.-F. Yu, D.-X. Tian, W.-C. Li, B. He, Y. Zhang, Z.-Y. Chen, A.-H. Lu, *Nano Res.* **2019**, *12*, 1193.
- [40] J. Zhang, J.-Y. Li, W.-P. Wang, X.-H. Zhang, X.-H. Tan, W.-G. Chu, Y.-G. Guo, *Adv. Energy Mater.* **2018**, *8*, 1702839.
- [41] X. Hong, J. Jin, T. Wu, Y. Lu, S. Zhang, C. Chen, Z. Wen, *J. Mater. Chem. A* **2017**, *5*, 14775.
- [42] N. Pavlin, S. Hribernik, G. Kapun, S. D. Talian, C. Njel, R. Dedryvère, R. Dominko, *J. Electrochem. Soc.* **2018**, *166*, A5237.
- [43] X. Chen, H.-J. Peng, R. Zhang, T.-Z. Hou, J.-Q. Huang, B. Li, Q. Zhang, *ACS Energy Lett.* **2017**, *2*, 795.
- [44] X. Chen, X. Ding, C. Wang, Z. Feng, L. Xu, X. Gao, Y. Zhai, D. Wang, *Nanoscale* **2018**, *10*, 13694.
- [45] Y. Luo, N. Luo, W. Kong, H. Wu, K. Wang, S. Fan, W. Duan, J. Wang, *Small* **2018**, *14*, 1702853.
- [46] S. Huang, Y. V. Lim, X. Zhang, Y. Wang, Y. Zheng, D. Kong, M. Ding, S. A. Yang, H. Y. Yang, *Nano Energy* 2018, 51, 340.
- [47] Y. Qiu, W. Li, W. Zhao, G. Li, Y. Hou, M. Liu, L. Zhou, F. Ye, H. Li, Z. Wei, S. Yang, W. Duan, Y. Ye, J. Guo, Y. Zhang, *Nano Lett.* **2014**, *14*, 4821.
- [48] Z. Yuan, H.-J. Peng, T.-Z. Hou, J.-Q. Huang, C.-M. Chen, D.-W. Wang, X.-B. Cheng, F. Wei, Q. Zhang, *Nano Lett.* **2016**, *16*, 519.
- [49] S. Chen, J. Luo, N. Li, X. Han, J. Wang, Q. Deng, Z. Zeng, S. Deng, *Energy Storage Mater.* **2020**, *30*, 187.
- [50] Y. Li, P. Xu, G. Chen, J. Mou, S. Xue, K. Li, F. Zheng, Q. Dong, J. Hu, C. Yang, M. Liu, *Chem. Eng. J.* **2020**, *380*, 122595.
- [51] W. Tian, B. Xi, Z. Feng, H. Li, J. Feng, S. Xiong, *Adv. Energy Mater.* **2019**, *9*, 1901896.

- [52] Z. Du, X. Chen, W. Hu, C. Chuang, S. Xie, A. Hu, W. Yan, X. Kong, X. Wu, H. Ji, L.-J. Wan, *J. Am. Chem. Soc.* **2019**, *141*, 3977.
- [53] F. Y. Fan, W. C. Carter, Y.-M. Chiang, Adv. Mater. 2015, 27, 5203.
- [54] H. Yuan, H.-J. Peng, B.-Q. Li, J. Xie, L. Kong, M. Zhao, X. Chen, J.-Q. Huang, Q. Zhang, *Adv. Energy Mater.* **2018**, 1802768.
- [55] Y. Pan, X. Cheng, M. Gao, Y. Fu, J. Feng, H. Ahmed, L. Gong, H. Zhang, V. S. Battaglia, *ACS Appl. Mater. Interfaces* **2020**, *12*, 32726.
- [56] R. Wang, C. Luo, T. Wang, G. Zhou, Y. Deng, Y. He, Q. Zhang, F. Kang, W. Lv, Q. Yang, *Adv. Mater.* **2020**, 2000315.
- [57] Y. Yan, Z. Chen, J. Yang, L. Guan, H. Hu, Q. Zhao, H. Ren, Y. Lin, Z. Li, M. Wu, *Small* **2020**, *16*, 2004631.
- [58] X. Zhu, W. Zhao, Y. Song, Q. Li, F. Ding, J. Sun, L. Zhang, Z. Liu, *Adv. Energy Mater.* **2018**, *8*, 1800201.
- [59] G. Zhou, H. Tian, Y. Jin, X. Tao, B. Liu, R. Zhang, Z. W. Seh, D. Zhuo, Y. Liu, J. Sun, J. Zhao, C. Zu, D. S. Wu, Q. Zhang, Y. Cui, *Proc. Natl. Acad. Sci.* **2017**, *114*, 840.
- [60] A. Eftekhari, Sustain. Energy Fuels **2017**, 1, 2053.
- [61] Y. V. Mikhaylik, J. R. Akridge, J. Electrochem. Soc. **2004**, 151, A1969.
- [62] A.-H. Shao, Z. Zhang, D.-G. Xiong, J. Yu, J.-X. Cai, Z.-Y. Yang, *ACS Appl. Mater. Interfaces* **2020**, *12*, 5968.

Table of Contents (TOC)





Tubular CoFeP@CN Mott-Schottky Catalyst